Surface & Coatings Technology 375 (2019) 22–33

Contents lists available at ScienceDirect

Surface & Coatings Technology

journal homepage: www.elsevier.com/locate/surfcoat

Quantification of the interfacial roughness when coating stainless steel onto aluminium by friction surfacing

M.J.R. Stegmueller[a,*], R.J. Grant[a], P. Schindele[b]

[a] Western Norway University of Applied Sciences, Dept. Mechanical and Marine Engineering, Norway
[b] Kempten University of Applied Sciences, Dept. Mechanical Engineering, Germany

ARTICLE INFO

Keywords:
Friction surfacing
Inductive heating
Stainless steel
Interfacial roughness
Push-off test
Shear test
Bond strength

ABSTRACT

Friction surfacing offers a means of producing coatings between dissimilar materials through a solid state process; a union that would otherwise be classed as incompatible for liquid state coating processes. A method of using a rotating consumable friction rod supplemented by inductive heating was employed to produce conditions necessary for a sound bond between a stainless steel coating and an aluminium substrate. The rotational speed of and load on the coating rod influenced the bond strength significantly with low rotational speeds and high load values producing a good bond quality; however, cavitations at the coating-substrate interface showed a detrimental effect on the bond quality. Mechanical interlocking could be identified from images of longitudinal cross-sectional slices which were recorded using optical microscopy. An image recognition software tool was used to generate an interfacial roughness profile graph which described the coating-substrate interface. Additional filtering of the profile graph showed the depth of mechanical interlocking of the stainless steel coating into the aluminium substrate with the degree of this interlocking quantified by roughness values calculated from the profile graph. Large roughness values can be related to high coating push-off strengths (up to 107 MPa), and also were a result of low rotational speeds and high load values during friction surfacing. Dovetail shaped mechanical interlocks identified in the profile produced both high push-off and shear strength when compared with wedge-shaped interlocks; which, overall, provided good shear strengths up to 126 MPa.

1. Introduction

Friction surfacing is a coating procedure which is derived from the joining process of friction welding [1]. During friction surfacing a rotating consumable rod is pressed onto and traversed along a substrate material to deposit a layer or coating. Multilayer coatings can be produced by overlapping adjacent layers and can provide a wear resistant surface with an absence of bonding defects [2]. By way of example, applications for friction surfacing may align themselves with the coating of marine components and Murugan et al. showed that a copper-nickel-iron alloy (MONEL) can be coated onto carbon steel [3]. In the aircraftsector, turbine blade roots can be coated with titanium alloys [4].

In recent years, an increasing number of publications have presented results of research directed at gaining an understanding of the friction surfacing process and the associated substrate-coating bonding mechanisms. The material groupings whereby stainless steel [5,6], cold work steel [7], and aluminium [8,9] were coated onto a mild steel substrate have been investigated more frequently than other combinations. Typically, specimens have been subject to detailed research concerning the modelling of the process, performance analysis, metallurgical characterisation, corrosion testing [6], and bond strength determination [10].

Hybrid technologies, such as combining friction surfacing with friction stir welding, have shown the technique capable of producing high quality mixed metal joints between aluminium and titanium for possible application in both the aviation and automotivesectors [11].

The more exotic material combination of stainless steel coatings on aluminium substrates had not been investigated beyond the work presented by Chandrasekaran et al. [12,13], until the recently published work of the current authors [14,15]. It was previously claimed that the coating of stainless steel onto an aluminium substrate was problematic as no intermetallic compound could be found at the coating-substrate interface; which was accompanied by gaps, cracks, and a lack of mechanical interlocking reducing the bond quality significantly [12]. The coating mechanism was described using the analogy of rod filaments which were sheared-off from the rotating coating rod and then rolled into the aluminium substrate.

* Corresponding author.
E-mail addresses: mjrs@hvl.no (M.J.R. Stegmueller), rjg@hvl.no (R.J. Grant), paul.schindele@hs-kempten.de (P. Schindele).

https://doi.org/10.1016/j.surfcoat.2019.06.060
Received 6 May 2019; Received in revised form 19 June 2019; Accepted 20 June 2019
Available online 27 June 2019

Table 1
Chemical composition and material properties of AlMgSi alloy EN AW 6060 (DIN EN 573-3) and stainless steel X5CrNi18-10 alloy EN 1.4301 (DIN EN 10088-1).

Numerical	Chemical	Si	Fe	Cu	Mn	Mg	Cr	Ni	Zn	TiGa	V
EN AW-6060	EN AW-Al MgSi	0.30–0.6	0.10–0.30	0.1	0.1	0.35–0.6	0.05	–	0.15	0.1	–

Numerical	Chemical	C	Si	Mn	P	S	Cr	Mo	Ni	N	Cu	Nb
1.4301	X5CrNi18-10	0.07	1	2	0.045	0.015	17.5–19.5	–	8–10.5	0.1	–	–

On the other hand, the interface between a mild steel coating and an aluminium substrate has been shown to provide both the formation of a thin interfacial phase and mechanical interlocks [12].

For the austenitic stainless steel coating AISI316 (X5CrNiMo17-12-2) on a mild steel substrate the process of dynamic recrystallization could be observed for the coating material and resulted in an increased occurrence of intergranular martensitic features in the austenitic matrix. Scanning electron microscopy showed no evidence of alpha ferrite which resulted in improved corrosion resistance of the coating [6].

Guo et al. showed the improvement of the coating hardness and its pitting corrosion resistance for the stainless steel 316L (X2CrNiMo17-12-2) when coated onto stainless steel 304 (X5CrNi18-10) substrates [16]. The improvements of the microstructure could be observed for an increase in rotational speed of the coating rod only on the coating surface when compared with the microstructure in the cross section near the bonding interface. The increased rotational speed resulted in a higher degree of grain refinement and hardness at the coating surface. From a detailed standpoint, the chemical compound of MnS was fragmented and increased the pitting corrosion resistance.

The coating of aluminium (AlMg4.5Mn) onto a DH36 steel plate resulted in the formation of the intermetallic phase $FeAl_3$ which was attributed to a diffusion mechanism at the coating-substrate interface [9]. In this work by Li et al., the intermetallic phase was reported to be accompanied by cracks and gaps at the interface between the coating and substrate; which propagated and instigated delamination of the coating when conducting bend tests.

A further material combination for applications in a corrosive environment is presented by Hanke et al. [17] whereby nickel based alloy 625 is coated onto a steel substrate (42CrMo4) for repair applications. Specifically in the oil and gas industry, low cost basic grade steel components can require surface property improvements by corrosion resistant coatings. Investigation of the coating showed grain refinement and dynamic recrystallization caused by high strain rates during friction surfacing. The authors concluded that friction surfacing offers the potential to study the changes in material properties under high strain and high strain rates.

A more detailed review on the microstructural evolution of various materials being coated, including multi-layer coatings (i.e. aluminium, steel, and NiAl-bronze) can be found in the review by Saw et al. [18]. However, the review does not provide any information on the bonding mechanisms involved between coated layer and substrate.

The dominant bonding mechanisms between a steel coating and a steel substrate is described as being principally by diffusion [19] and also by supplemental mechanical interlocking [20]. However, for specimens that were characterised by interlocking being a dominant bonding mechanism, the degree of mechanical interlocking was not quantified.

It has been shown recently, by the authors of this current work, that stainless steel can be bonded onto aluminium substrates by the application of a technique involving the additional inductive heating of the coating rod; a procedure that provides the conditions necessary to create an increased bonding quality [14]. In this article, the authors would like to show that an interfacial roughness value can be determined from longitudinal cross-sections of specimens produced by friction surfacing with additional inductive heating. The objective is to correlate the roughness values with the bond strength determined by a particular bond strength test. The aim is to determine whether chemical bonding or pure mechanical interlocking is to be regarded as a main bonding mechanism when coating stainless steel onto aluminium substrates.

2. Material and methods

The basic austenitic stainless steel EN 1.4301 (AISI304, X5CrNi18-10), used as the coating material, provides both good weldability and corrosion resistance properties [21]. The material offers weak ferromagnetic characteristics due to a limited volume-percentage of ferrite, which is of advantage as it permits the use of inductive heating of the coating rods [22]. Drawn rods (grain size K140) ground to a diameter d = 10 mm and cut to a length of 90 mm were employed for the study. Flow curves for the steel show increasing yield stresses at higher strain rates and the change of the Young's modulus against temperature decreases by about 40% when the temperature is increased from 0 to approximately 800 °C. The deformation of the stainless steel rod in hot conditions results in the continuous process of generating and storing, as well as rearranging and annihilating, dislocations during dynamic recovery [23].

The wrought substrate material EN AW6060 (AlMgSi0.5) employed in the trials offers artificial ageing properties due to precipitation hardening effects of Mg2Si segregates. The substrate dimensions were 20 × 6 × 135 mm and a steel 'start plate' (mild steel) with dimensions 20 × 6 × 30 mm was employed as suggested by Chandrasekaran et al. [12]. The friction surfacing process was initiated on the steel start plate and the coating then was extended onto the aluminium substrate. Chemical compositions of both materials are presented in Table 1. All the materials used were degreased before the coating process commenced. The weight and dimensions of both the coating and substrate were documented before and subsequent to the friction surfacing.

Friction surfacing was accomplished by employing a modified milling machine which applied the required load onto the rotating rod via a pneumatic cylinder. Constant inductive heating was provided at the tip of the coating rod with an inductive unit power of 5 kW. The design of experiment was developed using four values for both rotational speed (3000, 4000, 5000, and 6000 rpm) and pneumatic cylinder pressure (5, 6, 7, and 8 bar) for a constant coating rod travel (traverse) speed of 150 mm/min. For each parameter combination three separate specimens were produced to gain a higher statistical significance. Hardness values were measured before and after friction surfacing across the cross-section of the specimens, using a Vickers micro hardness test machine (Buehler Indentamed 1104). This unit provided *HV*0.5 values, which equated to a test load of about 5Nfor both the aluminium and stainless steel substrate. Up to six indentations were produced on the substrate and also on the coating near the interface. So as to exclude the influence of strain hardening effects produced as a result of an adjacent indentation an inter-indentation distance of 0.6 mm on aluminium and 0.3 mm on stainless steel was considered appropriate [24].

The bond strength of the specimens was determined for both shear and push-off loading of the coating as proposed by Khalid et al. [25] and Voutchkov et al. [26], respectively. The method comprises the

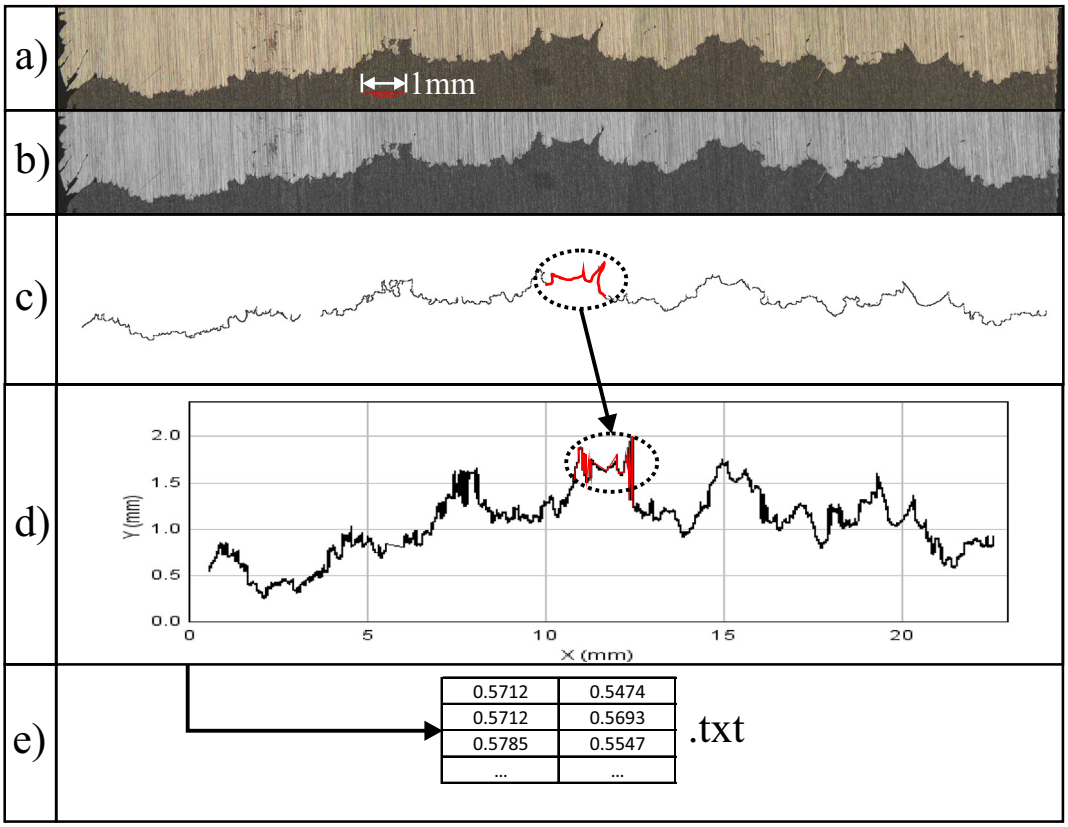

Fig. 1. Manipulation of the longitudinal cross-section and corresponding flow chart: a) Longitudinal cross-section, b) conversion to an 8-bit greyscale image, c) extraction of the coating-substrate interface, d) generation of a line graph, and e) extraction of values.

milling of test specimens to a specified geometry. For push-off testing the coating was milled to a cylinder and a hole was introduced into the substrate material from the back to push-off the coating by way of a pin. For shear testing the coating was milled into a rectangular shape and then sheared-off along the coating length. A more detailed description of these testing methods can be found in a previous publication by the current authors [14]. The bond test setup was installed in a universal tensile testing machine (Zwick Roell RKM200). Longitudinal and transversal cross-sections were produced from the coated specimens by grinding down to a grain size of 8.4μm and subsequently polished with a suspension providing 6 and 3μm grains. Optical microscopy (Olympus BX51M) was employed for initial investigations of the cross-sections.

3. Determination of the interfacial roughness values

In a previous study conducted by the authors of this work [14] specimen cross-sections were produced that revealed a coating-substrate interface with a certain degree of mechanical interlocking (see Fig. 1a)). It was thought that the quality of the bonding at this interface may be related to the geometry of the interconnection; which in turn, could be defined by the height (penetration depth) and distance of the peaks visible in the cross-section. The profile could then be compared with a roughness profile derived from a surface topography.

To that end, an image recognition tool was used to extract the *interfacial roughness profile graph* of the coating-substrate interface and then the specific values that could be used described the height and distance of the profile peaks from one another were calculated. These values were then compared with the bond strengths in order to determine a possible relationship between interfacial roughness and the bond strength.

This section provides details on the approach to determine the interfacial roughness values from the interfacial roughness profile graph. The images of the specimen cross-sections were manipulated in the software tool *ImageJ* [27] so that a profile graph was created whose X-Y-values were then loaded into an array. These values were then processed by a program, which utilised the programming language *Python* [28] and was applied at a specified dimensional interval along the length of a series of the specimens' longitudinal cross-sections.

Fig. 1 illustrates the steps taken in the image processing software to manipulate the images of the specimens. The cross-sectional image was imported into *ImageJ* as a TIF (Tagged Image Format) file and the scale function was applied to convert the constituent pixels into dimensional coordinates (Fig. 1a)) where millimetres were chosen. The *RGB* (Red Green Blue) image was converted into an 8 bit grey scale image from which the coating-substrate interfacial line was extracted by application of the *Image Edge* (for *ImageJ*) plug-in (Fig. 1b)). The interfacial line was discontinuous at locations where the plug-in could not detect an edge, which was caused by the lack of contrast between neighbouring grey values. This lack of contrast was a result of unevenly ground cross-sections or by surface-substrate contamination, where the aluminium material was carried-over to the stainless steel by the grinding.

Images were manually â€™cleanedâ€™ from pixels that were a product of scratches on their cross-section, created during grinding of the specimens; scratches were misinterpreted by the image algorithm as representing an edge. In the next step, the image was converted into a binary format that only contained black (value 255) and white (value 0) pixels (Fig. 1c)) and enabled the use of the *Analyze Line Graph* tool [29]. This algorithm recognises the black pixels and assigns each pixel a coordinate in the X-Y Cartesian system (Fig. 1d)). One difficulty that arose was that the tool assigned two or more Y-values to one X-value at the position where an undercut was present (see example in Fig. 2a), b), and c)); therefore, only the size of the vertical dimension (material thickness) and not the shape of an undercut could be considered for subsequent evaluation. With this method mechanical interlocks could

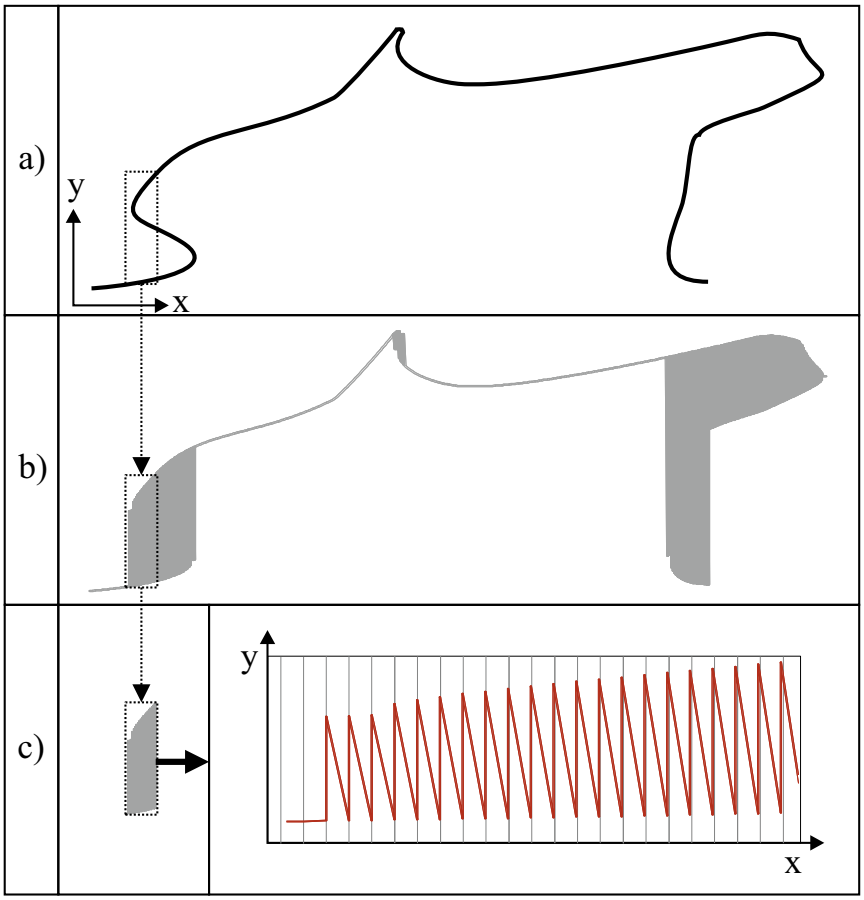

Fig. 2. Manipulation of the roughness profile applying the ALG tool: a) example of a roughness profile gained from a cross-section, b) graph produced by the ImageJ ALG tool, and c) magnified section of the graph.

only be identified by their penetration depth into the substrate and coating, and not by their degree of interlocking within either the substrate or coated layer. Linear interpolation was employed by the tool on locations where the interfacial line was discontinuous.

Finally, the X-Y-coordinates extracted were saved into a *.txt* file (Fig. 1e)), column and line separated, ready for further processing in the python shell. It should be noted that a scatter in the profile values generated could be introduced through a variation in grey values at the coating-substrate interface. The accuracy in the recognition of the interface was dependent on the image quality which was a little inconsistent as the cross-sections were prepared manually.

The surface of a manufactured object provides a certain roughness profile, which can be measured using a stylus as it is moved over the surface by a defined distance. However, in this investigation of the interfacial roughness, the stylus was replaced by the *ImageJ Image Edge* algorithm.

The roughness profile in a time or spatial domain can be seen as a collection of sinusoidal functions with different wavelengths and amplitudes; various wavelengths can be filtered to gain different information on the object measured. The overall geometrical form of a given surface, which forms the part, provides long wavelength values and should not contribute to the surface roughness values [30]. Therefore, the acquired primary profile needs to be separated into 'form', 'waviness', and 'roughness' profiles which was accomplished employing a Fourier transformation. These profiles are dependent on the associated wavelengths. The classification of roughness and waviness by a defined wavelength of the surfaces is documented in standards (DIN-EN-ISO 11562) [31].

The flow chart for the python code development is presented in Fig. 3 which illustrates the necessary steps based on the separation of two superimposed triangular functions of different amplitudes (1 and 0.25 mm) and wavelengths (2 and 0.5 mm). The code permitted the production of both graphical and numerical output files. Two loops were employed in the Python code to go through a certain number of folders containing a defined number of interfacial roughness profile files: each file was associated with an individual cross-section prepared from the trials of the study.

The *.txt* files generated by *ImageJ*, were imported into the Python shell (see step 1. in Fig. 3) and then were separated into two arrays. One array contained all X-values (distance and width of profile peaks) and the other all Y-values (amplitude of the profile peaks) which was considered in step 2, Fig. 3.

After separation, the step-size on the X-axis and its reciprocal value (the sampling frequency) was determined describing the spacing between single data points as being of a constant value along the whole graph. The values were saved in another array, which was handled by step 3. in Fig. 3.

From the step-size array it could be noticed that *duplicates* of X-values were evident, causing a zero step-size value between two adjacent data points. The duplicates result from the undercuts in the profile, where two or more Y-values have been determined for a single X-value by the Analyze Line Graph algorithm. All duplicates were deleted resulting in a sequence of X-values with a defined step-size of 0.0073 mm. The reciprocal value of the step-size equates to the sampling frequency used, later-on, for the generation of wavelength values corresponding to the fast Fourier transformation (FFT) coefficients.

The FFT domain was created (see step 4. in Fig. 3) employing Eq. (1) [32]. In the FFT domain the profile was filtered leaving a certain frequency interval and removing defined high and low frequencies (step 5. and 6.). An inverse FFT python function was employed (step 7.) to

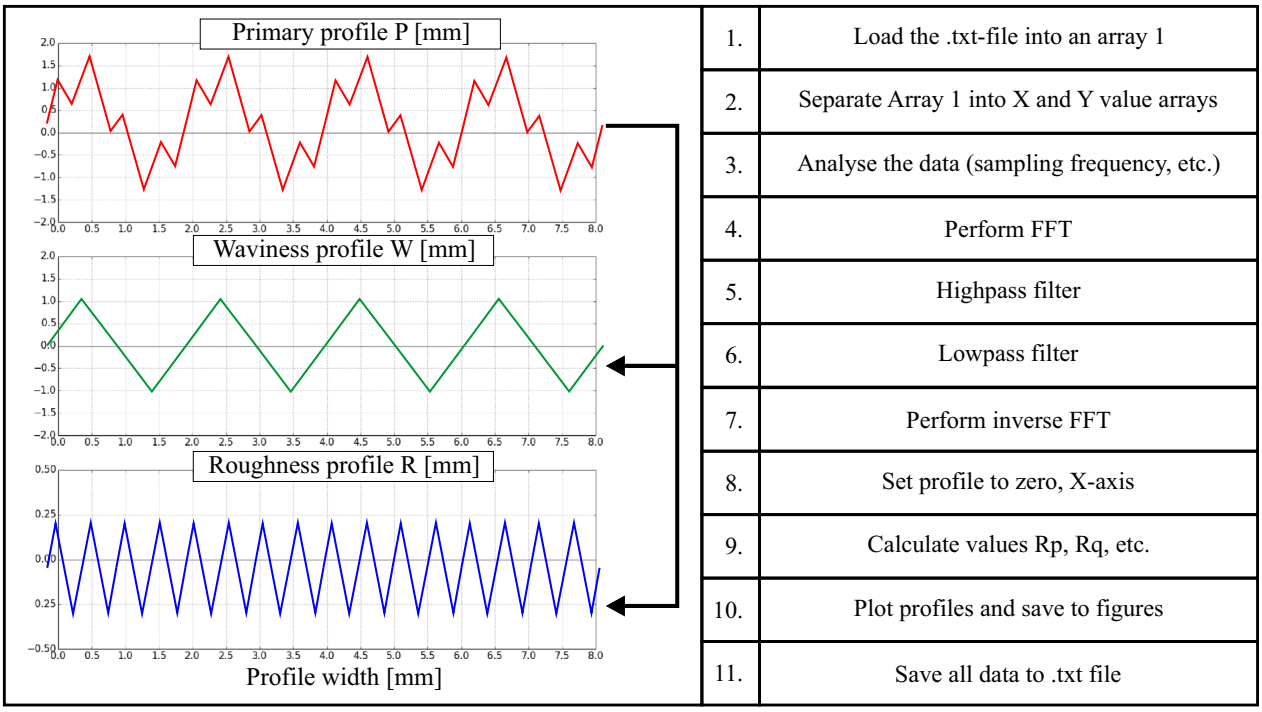

Fig. 3. Schematic representation of the primary profile filtering process: Separation of the primary profile (P) into waviness (W) and roughness (R) profiles based on two superimposed triangular functions.

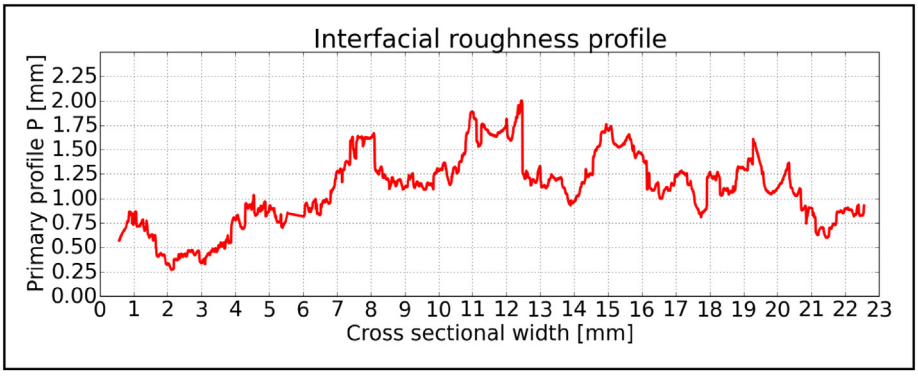

Fig. 4. Basic principle of the filtering method: obtained primary profile.

calculate the filtered values of the data. The mean Y-value of the profile curve was calculated and subtracted from each single Y-value to remove the profile offset from the zero X-axis (step 8.). The specific roughness values could then be calculated (step 9.) to quantify the dimensional size of the peaks and valleys. More information on step 5. to 9. are provided in Figs. 4 to 6. In step 10. and 11. all data is saved to *.txt* and image files.

$$f(x) \equiv s(x) = \frac{a_0}{2} + \sum_{k=1}^{\infty} (a_k \cdot coskx + b_k \cdot sinkx) \quad (1)$$

The Fourier analysis decomposes the function $f(x)$ into a discrete line spectrum containing discrete wavelengths and amplitudes.

The Y-values of the primary profile (see Fig. 4) are transformed into the FFT domain and now are represented by amplitudes and their associated decreasing wavelengths [30]. The initial value of the FFT array contains the coefficient a_0, which represents the *mean* value of all amplitudes (i.e. Y-values). If the value a_0 is subtracted from the profile Y-values, the *mean* of the roughness profile is shifted to zero; that is, it is congruent to the X-axis (see step 8. in Fig. 3).

To allow the elimination of specific wavelengths a filtering process was used which applied a zero multiplier to certain amplitudes (see Fig. 5). In the example given, a band-pass (high and low pass filtering) was employed: only letting wavelengths between certain values (e.g. between 0.1 and 1 mm) pass, which resulted in the indices of the wavelength entries that lie in-between these values to be written to a separate index array. This index array was then used to create the band-pass array, which showed a “1” at every entry of the wavelength to be passed.

Multiplication of the band-pass array with the FFT array removed all unwanted amplitudes, only preserving the selected ones. The FFT array created contained both real (cosine coefficients) and imaginary (sine coefficients) parts; represented as complex numbers associated with decreasing wavelengths. The second half of the array was a mirror of the first half. The FFT overall amplitude was calculated by the geometric sum of the sines and cosines.

It should be noted that the first entry of the array is a real number, the factor a_0, as shown in Eq. (1). By the application of the inverse Fourier algorithm (iFFT), the values are transformed back into the roughness/distance domain, showing a filtered profile, as presented in Fig. 6.

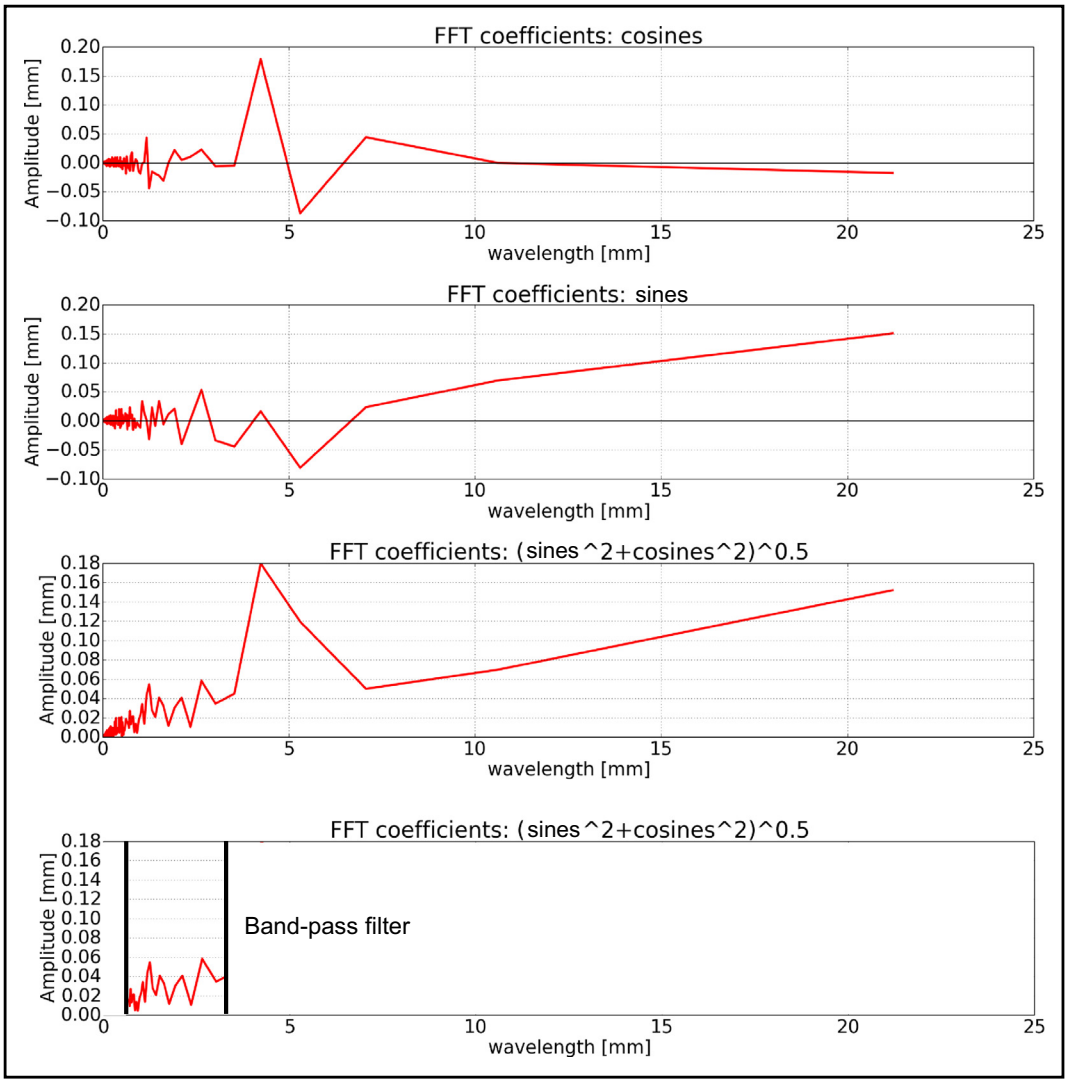

Fig. 5. Basic principle of the filtering method: FFT with corresponding cosines, sines, and overall coefficients in arrays multiplied with a band-pass filter array containing both "0" and "1" values.

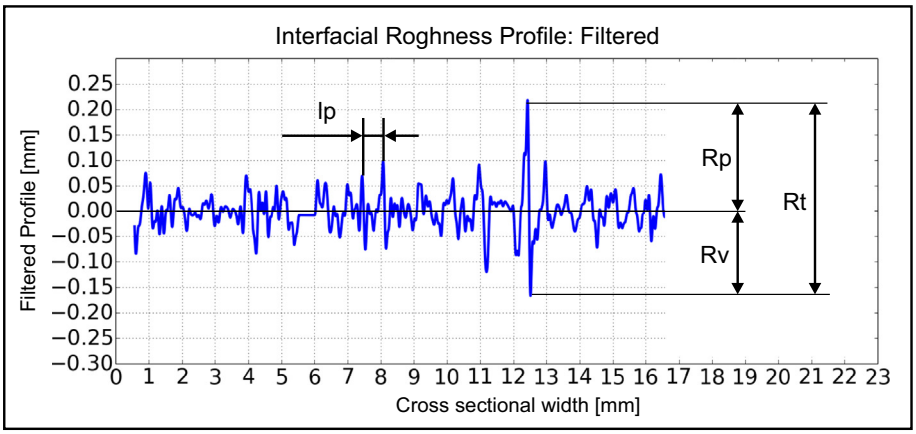

Fig. 6. Basic principle of the filtering method: filtered roughness profile after performing inverse FFT.

From the filtered roughness profile, the various roughness parameters (named R with a corresponding letter) can be calculated. The average roughness (Ra) is defined by the arithmetic mean of the absolute values measured from the mean line ($r(i)$), which is the X-axis, as shown in Fig. 6:

$$Ra = \frac{1}{n} \cdot \sum_{i=1}^{n} |r(i)| \tag{2}$$

The root-mean-square value is described by Rq:

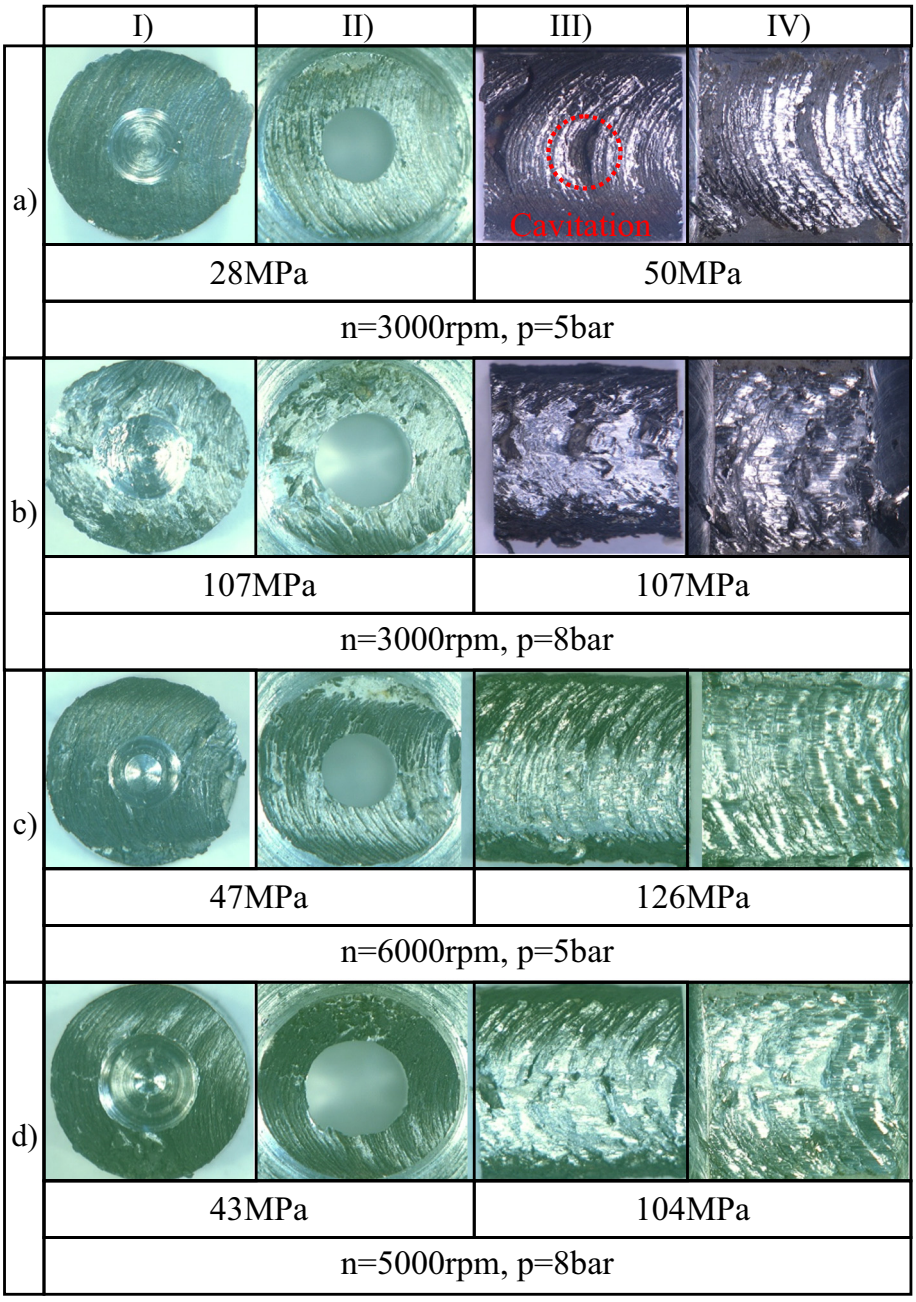

Fig. 7. Fractured surfaces and corresponding bond strength for different extreme values of rotational speed (*n*) and pneumatic cylinder pressure (*p*): I) pushed off coating and II) substrate; III) Sheared off coating and IV) substrate.

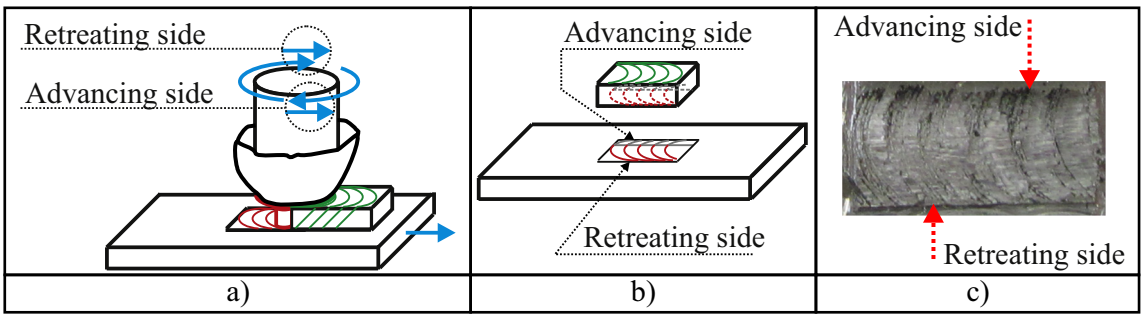

Fig. 8. Semicircular patterns at coating-substrate interface and coating surface: a) schematic illustration during coating, b) schematic illustration of sheared specimen, and c) actual specimen.

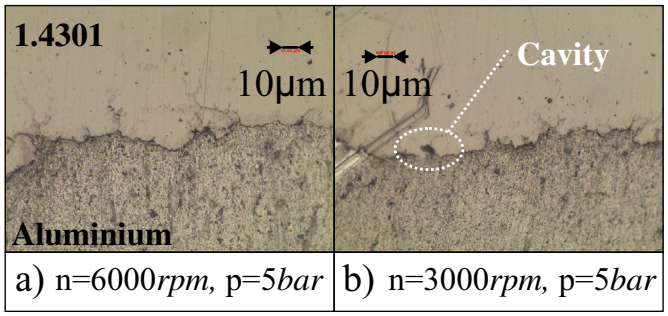

Fig. 9. Transverse cross-section of specimens, optical microscope 500×.

Table 2
Micro hardness values of both as received coating and substrate material before coating compared with DIN EN referenced values.

Material	As Received	*Vickers* [HV]	*Brinell* [HB]
Aluminium	Measured	81	76
Aluminium	DIN EN 755-2	–	75
1.4301	Measured	280	266
1.4301	DIN EN 10088-3	215	–

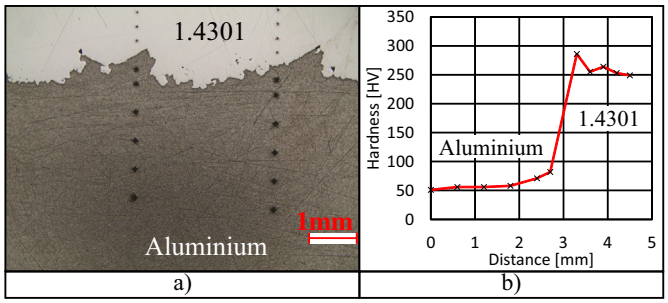

Fig. 10. a) Micro hardness indents on cross-section; b) corresponding graph with values.

$$Rq = \sqrt{\frac{1}{n} \cdot \sum_{i=1}^{n} r(i)^2} \tag{3}$$

The peaks (*Rp*) and valleys (*Rv*) of the profile can be described by an 'overall' or a 'local' value. 'Local' signifies that next to the peak value, the slope of the graph is positive on one side and negative on the other, whilst the 'overall' values give the extreme peak-to-valley values present for the entirety of the graph:

$$Rp = max(r) \tag{4}$$

$$Rv = |min(r)| \tag{5}$$

The absolute height of the profile (*Rt*) is described by summing up the overall highest peak and the overall absolute value of the deepest valley:

$$Rt = Rp + Rv \tag{6}$$

It was thought that the density of the mechanical interlocks along the coating length could possibly be an important bonding parameter which is defined by the mean distance $\overline{l_p}$ between local maxima in the roughness profile, thus:

$$\overline{l_p} = \frac{1}{n} \cdot \sum_{i=0}^{n} (X(Rp_{[i+1]}) - X(Rp_{[i]})) \tag{7}$$

4. Results and discussion

4.1. Bond strength

The bond strength was determined for shear and push-off loading for a magnitude at which the coatings fractured. To calculate the bond strengths, the measured maximum load necessary to cause the bond to fail was divided by the measured fractured area.

When comparing the extreme values produced by the trials, a clear relation between the fractured area and the bond strength could be established. Small roughness values and the presence of cavitations reduced both shear and push-off strengths, (see Fig. 7a)III) where a cavitation is visible within a shear test specimen and almost no aluminium material is removed from the substrate during push-off testing). This may be assigned to low pressure (5 bar) values and low rotational speeds (3000 rpm). High pressure (8 bar) and low rotational speed (3000 rpm) both result in very high shear and push-off strength values, as can be seen from the removed aluminium material in Fig. 7b). Fig. 7c) shows that high rotational speeds (6000 rpm) seem to improve the shear strength despite low pressure values (5 bar). High rotational speed and high pressure show the same characteristics, offering poor push-off strength, such as illustrated in Fig. 7d). The strength values may be increased by artificial ageing at a constant temperature of 170 C [33], which promotes the production of segregates in the aluminium substrate increasing the interfacial tensile strength by up to 80% of the bulk material strength [34]. A mixed mode fracture mechanism is evidenced from the fractured areas.

From the fracture areas of the shear tested specimens, the results presented by Bedford et al. [19] could be confirmed; namely, that the rod was not in contact with the aluminium substrate, but it was in frictional contact with the coating layer that has been produced. When the coating was removed mechanically from the substrate semi-circular striations were revealed on both the coating and substrate indicating the presence of the front and rear (relative to the traverse direction) of the rotating rod. Furthermore, the advancing side could be distinguished by a fractured area with various shades of grey, which is associated with poor bonding integrity. These features are illustrated in Fig. 8).

Push-off and shear strength values of a high magnitude were produced at 3000 rpm and 8 bar. Whilst low push-off and shear values can be found at 3000 rpm and 5 bar. High shear and low push off values could be obtained from both 5000 and 6000 rpm at 8 and 5 bar, respectively. This specific parameter setup is examined more closely during the following metallurgical investigations.

4.2. Metallurgical investigation

Overall, from interface sections taken transversely to the coating line and at intervals along the length of the specimen, good bonding quality is indicated; although the presence of small cavitations for all parameter combinations are evident (see Fig. 9a and b).

Micro hardness testing was conducted before (cross-sections prepared from a coating rod and a substrate plate, see Table 2) and after the coating process (see micro hardness graph in Fig. 10). When comparing the values in Table 2 with the values from the graph in Fig. 10 it shows decreasing hardness for aluminium and increasing hardness for stainless steel after coating and near the coating to substrate interface. In *DIN EN 755-2* a hardness of 75HB is documented for the aluminium alloy used, whereas *DIN EN 10088-3* provides a value of 215 HV for stainless steel. It might be that the heat influence of the process reduces the hardness of the aluminium substrate significantly, whilst the stainless steel hardness is increased by a relatively smaller amount. Despite fast cooling rates during the coating process, temperatures at the coating rod tip still exceeding 1300 °C, which might cause local melting of the aluminium.

The micro hardness graph in Fig. 10 reveals that the maximum

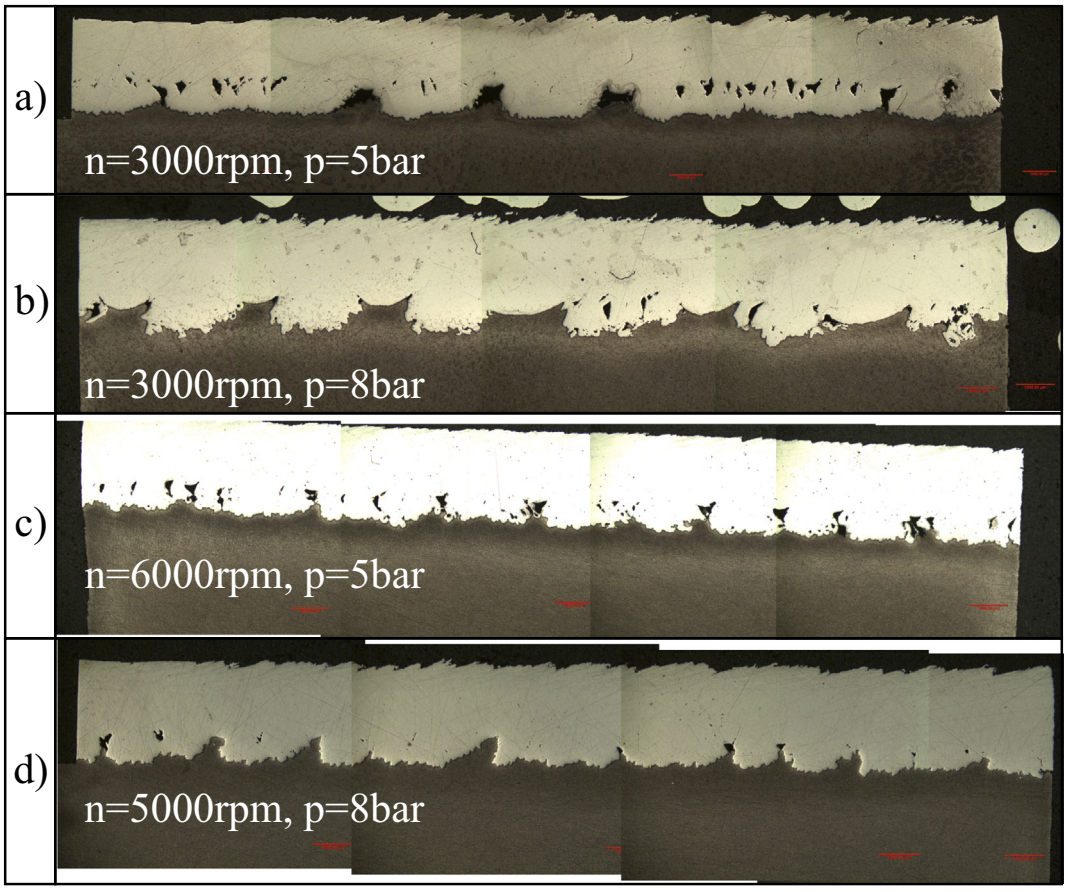

Fig. 11. Longitudinal cross-sections (magnification 25×) for different extreme values of rotational speed (n) and pneumatic cylinder pressure (p).

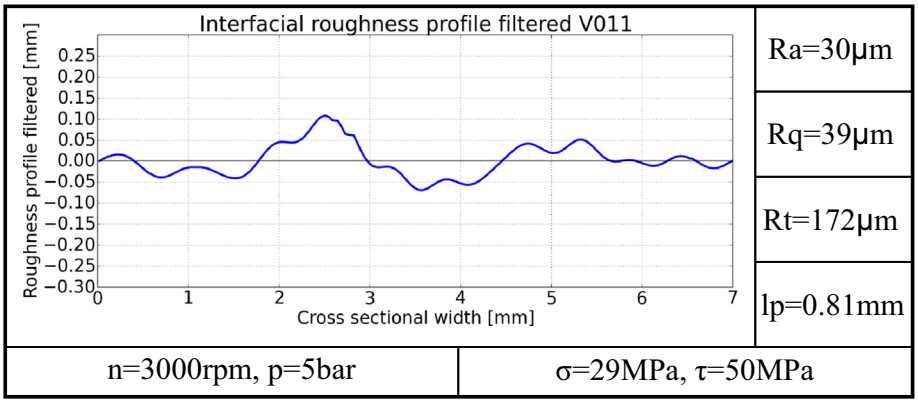

Fig. 12. Roughness profile, corresponding push-off strength (σ), and shear strength (τ) for rotational speed (n) 3000 rpm and pneumatic cylinder pressure (p) 5 bar by filtering wavelengths between 0.5 and 4 mm.

hardness is produced next to the interface in the coating; then the hardness drops towards the coating surface. The slight increase of aluminium hardness near the interface may be caused by work hardening, due to the hot coating material being pressed into the aluminium substrate; which stands in contradiction to an expected decrease in strength due to the lack of precipitation hardening effects related to very fast cooling rates. The increase in hardness near the bonding interface was also observed by Sahin [35] during friction welding of stainless steel and aluminium.

Longitudinal cross-sections (cut in the traverse direction of the coating rod) were prepared by cutting the specimens from the central sectional plane. What was revealed using an optical microscope was a varying degree of mechanical interlocking and the presence of cavitations (Fig. 11). The cavitations were seen to be either present in the bulk coating material or at the coating-substrate interface.

Increasing rotational speed at constant pressure resulted in a finer distribution of mechanical interlocks, as increasing pressure at constant rotational speed tends to fill up the cavitations present in the coating with substrate material; cavitations are more likely to occur in the coating when specimens are produced at low pressure values. This phenomena may be explained by considering the sheared off plasticized layers as they are pressed into the aluminium substrate which will not be subject to such a degree of compaction. The best bonding integrity was achieved at 3000 rpm and at an 8 bar cylinder pressure; these specimens showed the presence of undercuts, which were filled-up almost completely with substrate material. A certain degree of substrate

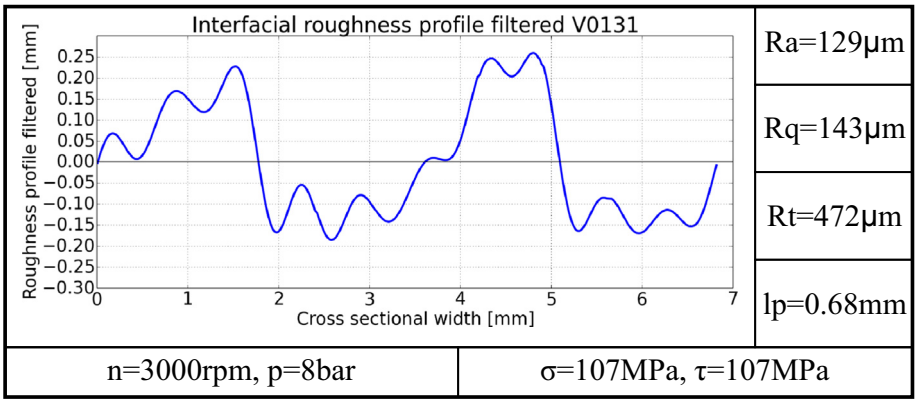

Fig. 13. Roughness profile, corresponding push-off strength (σ), and shear strength (τ) for rotational speed (n) 3000 rpm and pneumatic cylinder pressure (p) 8 bar by filtering wavelengths between 0.5 and 4 mm.

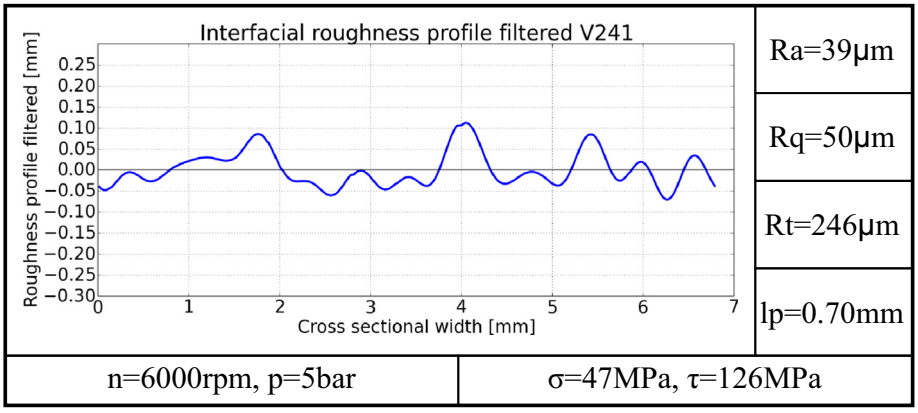

Fig. 14. Roughness profile, corresponding push-off strength (σ), and shear strength (τ) for rotational speed (n) 6000 rpm and pneumatic cylinder pressure (p) 5 bar by filtering wavelengths between 0.5 and 4 mm.

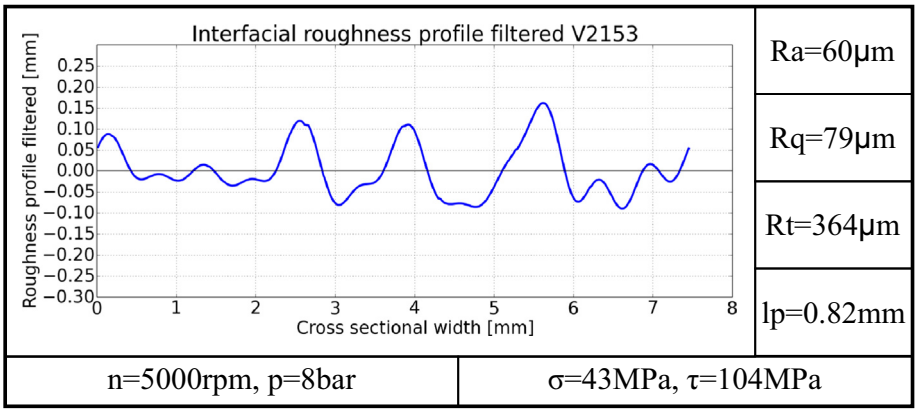

Fig. 15. Roughness profile, corresponding push-off strength (σ), and shear strength (τ) for rotational speed (n) 5000 rpm and pneumatic cylinder pressure (p) 8 bar by filtering wavelengths between 0.5 and 4 mm.

deformation is evident at the interface where the coating material was pressed into the substrate, which can be better visualised in the roughness profiles of Figs. 12 to 15. The form of the interlocks vary when comparing the dovetail profiles in Fig. 11b which produce high push-off values, with the wedge-shapes of Fig. 11d, which provide poor push-off values.

The interface profiles seem to be influenced by the process input parameters of rotational speed and pneumatic cylinder pressure which have a significant influence on the push-off strength values, as can be seen in Fig. 7. However, the influence of the interlocking shape on the shear test values is shown to be insignificant; on the other hand, the height, i.e. the penetration of the interfacial profile peaks of the substrate into the coating result in an increase in the shear strength.

4.3. Interfacial roughness

There were three specimens available per parameter combination. However, from each specimen four sub-specimens were prepared; that is, a push-off, a shear test, a transversal cross-section, and a longitudinal cross-section specimen. The longitudinal cross-section was employed for acquiring the interfacial profile graph. Coating parameters with increased pressure values resulted in a decreased coating length. So for

some parameter combinations a length of only 7 mm along the coating could be considered and prepared for the interfacial roughness investigation. This minimum length was set as the length considered for all specimens. The interfacial roughness was determined by calculating roughness values for three different profile types (classed as 'smoothed', 'courser' and 'waviness'), with each profile type being produced by employing three different filters with three different values for the wavelength.

The 'smoothed' roughness profile was obtained by removing all wavelengths outside the interval from 0.1 to 1 mm. The 'waviness' roughness profile was attained from filtering wavelengths between 2 and 8 mm. Both 'smoothed' and 'waviness' profile showed negligible difference in their roughness parameters for a variation of the coating process input parameters and are thus not considered for further investigations.

The 'courser' roughness profile was provided by filtering wavelengths from 0.5 to 4 mm and the profile delivered various roughness parameters for different input parameters. So this wavelength was employed for further investigation.

Figs. 12 to 15 present the roughness profile. It can be seen that a cross-section containing more cavities offers a finer roughness profile, whereas mechanical interlocks with increased dimensions and a minimum number of cavities provide larger roughness parameter values, i.e. a high penetration depth of the coating into the substrate.

The shape of the mechanical interlocks, which in some cross-sections provide a large degree of interlocking, cannot be represented in the roughness profile; although, the profile of the interlocks influence the bond strength to a certain degree. However, the degree of coating penetration into the aluminium substrate can be determined with the specimens showing a maximum penetration depth of about 0.2 mm. High coating rod pressures resulted in increased roughness values and high push-off strength, which can be seen when Fig. 7b and d is compared with both Figs. 13 and 15. There is no evidence relating these roughness parameters and the shear strength values. The surface roughness of the as-received aluminium substrate is about $Ra = 1.5\mu m$ which might be regarded as being insignificant when compared with the, much larger, interfacial roughness values determined. The distance between profile peaks (l_p) shows only a slight decrease at 3000 rpm and 8 bar which would suggest that it is an insignificant parameter.

5. Conclusions

1. The novel approach to determine the interfacial roughness profile from a coating-substrate interface was able to resolve and represent the variation in interfacial topology. The coating penetration into the substrate material was ascertained by filtering wavelengths (0.5 to 4 mm) of the primary roughness profile.
2. Good bonding quality concerning shear and push-off strength, both up to a mean value of 107 MPa, was obtained for a coating rod rotational speed of 3000 rpm, a pneumatic cylinder pressure of 8 bar, and a travel speed of 150 mm/min. This parameter combination was linked to large roughness values.
3. Push-off specimen fractures occurred as mixed mode failures, both at the interfacial coating-substrate zone and in the aluminium substrate.
4. Mechanical interlocking varied in its dimension and shape; where dovetail profiles caused both high push-off and shear strength values, whilst wedge shapes resulted in poor push-off and high shear strength values. The specific shape could not be acquired by the interfacial roughness profile from the methodology used in this study and needs to be considered for further work; however, the penetration depth of the stainless steel coating into the aluminium was determined with the help of interfacial roughness parameters and was linked to push-off strength values.
5. As the bond strength values have been determined only at a certain position along the coating length, such values do not provide information of the overall bond strength variability of the specimen. Evidence of the topological variation from the sectional images suggests that a coating bond quality may also correspondingly vary, resulting in higher or lower shear and push-off strength values. Three dimensional computer tomography and the determination of three dimensional roughness parameters might present a way of delivering more information on the overall bond quality of the coated layer.

Acknowledgments

The authors would like to thank Matthias Stiefenhofer and Bernd Pinzer for their support in this work.

References

[1] K.H. Stern, Metallurgical and Ceramic Protective Coatings, 1st edition, Chapman & Hall, London and, New York, 1996.
[2] D. Pereira, J. Gandra, J. Pamies-Teixeira, R.M. Miranda, P. Vilaça, Wear behaviour of steel coatings produced by friction surfacing, J. Mater. Process. Technol. 214 (12) (2014) 2858–2868, https://doi.org/10.1016/j.jmatprotec.2014.06.003 (doi:10.1016/j.jmatprotec.2014.06.003).
[3] B. Kiruthi Murugan, V. Balusamy, R. Padmanaban, ICSO, 5th and 6th January 2017: Proceedings of 2017 11th International Conference on Intelligent Systems and Control (ISCO), IEEE, Piscataway, NJ, 2017, p. 2017.
[4] V. Fitseva, H. Krohn, S. Hanke, J.F. dos Santos, Friction surfacing of ti–6al–4v: process characteristics and deposition behaviour at various rotational speeds, Surf. Coat. Technol. 278 (2015) 56–63, https://doi.org/10.1016/j.surfcoat.2015.07.039 (doi:10.1016/j.surfcoat.2015.07.039).
[5] A.K. Singh, G.M. Reddy, K.S. Rao, Pitting corrosion resistance and bond strength of stainless steel overlay by friction surfacing on high strength low alloy steel, Defence Technology 11 (3) (2015) 299–307, https://doi.org/10.1016/j.dt.2015.06.002 (doi:10.1016/j.dt.2015.06.002).
[6] R. George Sahaya Nixon, B.S. Mohanty, R. Sathish, Friction surfacing of aisi 316 over mild steel: a characteriation study, Defence Technology 14 (4) (2018) 306–312, https://doi.org/10.1016/j.dt.2018.03.003 (doi:10.1016/j.dt.2018.03.003.).
[7] S. Hanke, M. Beyer, J. dos Santos, A. Fischer, Friction surfacing of a cold work tool steel—microstructure and sliding wear behavior, Wear 308 (1–2) (2013) 180–185. doi:https://doi.org/10.1016/j.wear.2013.06.017.
[8] B. Vijaya Kumar, G. Madhusudhan Reddy, T. Mohandas, Influence of process parameters on physical dimensions of AA6063 aluminium alloy coating on mild steel in friction surfacing, Defence Technology 11 (3) (2015) 275–281, https://doi.org/10.1016/j.dt.2015.04.001 (doi:10.1016/j.dt.2015.04.001).
[9] H. Li, W. Qin, A. Galloway, A. Toumpis, Friction surfacing of aluminium alloy 5083 on dh36 steel plate, Metals 9 (4) (2019) 479.
[10] J. Gandra, H. Krohn, R. Miranda, P. Vilaça, L. Quintino, J. dos Santos, Friction surfacing—A review, J. Mater. Process. Technol. 214 (5) (2014) 1062–1093.
[11] Y. Huang, Z. Lv, L. Wan, J. Shen, J. F. dos Santos, A new method of hybrid friction stir welding assisted by friction surfacing for joining dissimilar ti/al alloy, Mater. Lett. 207 (2017) 172–175. doi:https://doi.org/10.1016/j.matlet.2017.07.081 (doi:10.1016/j.matlet.2017.07.081).
[12] M. Chandrasekaran, A. Batchelor, S. Jana, Study of the interfacial phenomena during friction surfacing of aluminium with steels, J. Mater. Sci. 32 (32) (1997) 6055–6062.
[13] M. Chandrasekaran, A.W. Batchelor, J. Sukumar, Friction surfacing of metal coatings on steel and aluminum substrate, J. Mater. Process. Technol. 72 (72) (1997) 446–452.
[14] M. Stegmueller, P. Schindele, R.J. Grant, Inductive heating effects on friction surfacing of stainless steel onto an aluminium substrate, J. Mater. Process. Technol. 216 (2015) 430–439.
[15] M. Stegmüller Jr., R.J. Grant, P. Schindele, Improvements in the process efficiency and bond strength when friction surfacing stainless steel onto aluminium substrates, Proceedings of the Institution of Mechanical Engineers, Part L: Journal of Materials: Design and Applications 78 (2017), https://doi.org/10.1177/1464420717701494 146442071770149. (doi:10.1177/1464420717701494).
[16] D. Guo, C.T. Kwok, S. Chan, Spindle speed in friction surfacing of 316l stainless steel – how it affects the microstructure, hardness and pitting corrosion resistance, Surf. Coat. Technol. 361 (2019) 324–341, https://doi.org/10.1016/j.surfcoat.2019.01.055 (doi:10.1016/j.surfcoat.2019.01.055).
[17] S. Hanke, J.F. dos Santos, Comparative study of severe plastic deformation at elevated temperatures of two aluminium alloys during friction surfacing, J. Mater. Process. Technol. 247 (2017) 257–267, https://doi.org/10.1016/j.jmatprotec.2017.04.021 (doi:10.1016/j.jmatprotec.2017.04.021).
[18] K. Saw, S. Shankar, S. Chattopadhyaya, P. Vilaca, Microstructure evaluation of different materials after friction surfacing - a review, Materials Today: Proceedings 5 (11) (2018) 24094–24103, https://doi.org/10.1016/j.matpr.2018.10.203 (doi:10.1016/j.matpr.2018.10.203).
[19] G.M. Bedford, V.I. Vitanov, I.I. Voutchkov, On the thermo-mechanical events during friction surfacing of high speed steels, Surf. Coat. Technol. 141 (1) (2001) 34–39 (141 (1)).

[20] M.L.K. de Macedo, G.A. Pinheira, J.F. dos Santos, T.R. Strohaecker, Deposit by friction surfacing and its applications, Weld. Int. 6 (24) (2010) 422–431 (6 (24)).
[21] R. Covert, A. Tuthill, Stainless steels: an introduction to their metallurgy and corrosion resistance, Dairy, Food and Environmental Sanitation (20 (7)).
[22] Information Service Stainless Steel, Information Sheet 827: Magnetic Properties of Stainless Steels, (2014).
[23] M. El Wahabi, J.M. Cabrera, J.M. Prado, Hot working of two aisi 304 steels: a comparative study, Mater. Sci. Eng. A 343 (1–2) (2003) 116–125, https://doi.org/10.1016/S0921-5093(02)00357-X (doi:10.1016/S0921-5093(02)00357-X).
[24] https://www.buehler.com/best-practices-rockwell-hardness-testing.php.
[25] H. Khalid Rafi, G. Janaki Ram, G. Phanikumar, Microstructure and properties of friction surfaced stainless steel and tool steel coatings, Mater. Sci. Forum 638-642 (2010) 864–869.
[26] I. Voutchkov, B. Jaworski, V.I. Vitanov, G.M. Bedford, An integrated approach to friction surfacing process optimisation, Surf. Coat. Technol. 141 (141) (2001) 26–33.
[27] W. Rasband, Imagej: Bethesda, maryland, usa (1997-2014). URL http://imagej.nih.gov/ij/.
[28] M. Lutz, Learning Python: Powerful Object-Oriented Programming, 5th edition, O'Reilly, Beijing, 2013.
[29] T. Ferreirad, R. Wayne, Imagej user guide, URL, 2014. http://imagej.nih.gov/ij/docs/guide/.
[30] B. Muralikrishnan, J. Raja, Computational Surface and Roundness Metrology, Springer, London, 2009.
[31] R. Volk, Rauheitsmessung-Roughness Measurement: Theorie Und Praxis, 1st edition, Praxis, Normung, Terminologie, Messwesen, Beuth, Berlin and Wien and Zürich, 2005 URL http://www.worldcat.org/oclc/76132844.
[32] H.-J. Bartsch, Taschenbuch Mathematischer Formeln- Handbook of Mathematic Equations, 20th edition, Fachbuchverl. Leipzig im Carl-Hanser-Verl, München and Wien, 2004.
[33] A.G. Austria Metall, Understanding early stages of precipitation in different 6xxx materials, AMAG customer and market information 1 (1) (2012) 16–17.
[34] F. Ostermann, Anwendungstechnologie Aluminium-Practical Application of Aluminium and its Alloys, 2nd edition, VDI-Buch, Springer, Berlin [u.a.], 2007.
[35] M. Sahin, Joining of stainless-steel and aluminium materials by friction welding, Int. J. Adv. Manuf. Technol. 41 (5–6) (2009) 487–497, https://doi.org/10.1007/s00170-008-1492-7 (doi:10.1007/s00170-008-1492-7).